Metallurgical and Materials Transactions A manuscript No.
(will be inserted by the editor)

Time-Temperature-Precipitation Relations for Nitrides and Evaluation of Internal Oxidation Theory for Nitridation of Austenitic Stainless Steel

Alice M. Young · Milo V. Kral · Catherine M. Bishop

Received: date / Accepted: date

Abstract Internal nitridation kinetics were determined for a UNS N08810/800H alloy using a general model of the form $x^n = kt$. Nitridation behavior was studied at service-relevant temperatures 800 °C–1000 °C in a 95% N_2/5% H_2 atmosphere for times 50 h–750 h. Optical and scanning electron microscopy were used for microstructural characterization and measurement of nitride penetration. AlN, Cr_2N, and CrN were formed, and the experimentally observed precipitation sequence was consistent with equilibrium calculations for this alloy using Thermo-Calc. A combination of diffusivity data determined using DICTRA and experimentally verified equilibrium calculations showed that Wagner's analysis for internal oxidation kinetics was valid for AlN penetration. Parabolic kinetics closely approximated measured AlN penetration. This suggests that extension of AlN penetration models to other temperatures and Fe-Ni-Cr-Al alloy systems is reasonable. Cr_2N penetration did not conform to Wagner's analysis. Deviation from parabolic behavior was evident, and general model penetration predictions for Cr_2N were experimentally validated. Using the experimentally determined models, time-temperature-precipitation diagrams for AlN and Cr_2N penetration were constructed.

Keywords Nitrides · Diffusion · Phase transformations · Austenitic stainless steel · Time-Temperature-Precipitation

Alice M. Young · Milo V. Kral · Catherine M. Bishop (corresponding author)

Dept. of Mechanical Engineering, University of Canterbury, Private Bag 4800, Christchurch 8041, New Zealand

E-mail: catherine.bishop@canterbury.ac.nz

1 Introduction

High-nickel, high-chromium, austenitic stainless steels are widely used in applications where resistance to both high-temperature corrosion and creep deformation is critical to performance [1]. In the petrochemical industry, Alloy 800H and its equivalents are the alloys of choice for steam reformer pigtail tubes, where service at temperatures 800 °C–900 °C for extended periods of time means that creep deformation is considered the primary failure mechanism [2]. Design lifetimes of 10 years or more necessitate good documentation of creep properties by suppliers, but failures have been known to occur after much shorter times in service (see e.g. [3–5]).

Internal oxidation is one of the damage mechanisms attributed with accelerating creep rate and reducing component life [6]. Diffusional ingress of sufficient quantities of an oxidising element results in formation of secondary precipitates, which can act as void nucleation sites [6]. Here, oxidation refers to the type of reaction, as the oxidising element is not necessarily oxygen. Nitrogen, carbon, and sulfur are also oxidants. Protection against this type of internal attack is achieved in high-temperature alloys by the addition of elements such as chromium and aluminium, which form protective oxide surface films [1]. However, large amounts of strain can cause the protective film to fracture and hence render the material vulnerable to internal oxidation [6]. Nitrogen can also cause internal attack with or without the presence of a protective oxide: chromia films are permeable to nitrogen [7,8]. Where a protective film is present, the rate of internal attack can be reduced due to slower mass transfer through the film in comparison to the base alloy [9,10].

Internal aluminium- and chromium-rich nitride precipitates have been found in decommissioned or failed pigtails that operated in air (see e.g. [2,4]). While final failure was generally attributed to other factors, there is evidence in the literature that nitrides alter the mechanical properties of steel, ductility in particular. For example, Wilson and Gladman's review [11] describes embrittlement and reduction in hot ductility of steels associated with AlN precipitation. Simmons [12] reports a severe reduction in room temperature tensile ductility and impact toughness due to Cr_2N precipitation in a high-nitrogen austenitic stainless steel. In both cases, the reduced ductility was attributed to formation of nitrides on grain boundaries, which created

initiation sites for grain boundary separation. Thomas and Smillie [2] stated that the reduction in ductility caused by formation of AlN in Alloy 800H pigtails can limit creep lifetime, but presented no experimental evidence as validation. A search of the literature indicates that the effects of nitride formation on creep behavior of Alloy 800H have not been tested.

Isolating the effects of nitride formation is difficult, but creep testing of pre-nitrided material is likely to give some insight. Such testing is the subject of future work, so models for nitride penetration kinetics are required to enable manufacture of test specimens in which the nitride precipitate front has reached a specified penetration depth.

1.1 Internal oxidation theory

A general model for the relationship between precipitate penetration depth x and time t is given in Equation 1, where n and k are constants.

$$x^n = kt \tag{1}$$

Wagner [13] derived parabolic kinetics ($n = 2$) for diffusion-controlled precipitation with an external source, such as occurs in oxidation, nitridation, and carburization. Equation 1 is then expressed as Equation 2, where $k_{(n=2)}$ is the parabolic rate constant.

$$x^2 = k_{(n=2)}t \tag{2}$$

Wagner's analysis [13] for a precipitation reaction $\mathrm{M} + \nu\mathrm{O} \rightarrow \mathrm{MO}_\nu$, where M is the least noble metallic element, leads to two limiting expressions for the rate constant (Equations 3 and 5). The appropriate expression is selected based on whether Inequality 4 or 6 is fulfilled. Given D_O is the bulk diffusivity of the oxidant in the matrix, $N_\mathrm{O}^{(s)}$ is the mole fraction of dissolved oxidant at the surface (taken to be the solid solubility of the oxidant in the matrix at the temperature and pressure of interest), D_M is the bulk diffusivity of M in the matrix, and $N_\mathrm{M}^{(o)}$ is the mole fraction of M in the bulk alloy, then

$$k_{(n=2)} = \frac{2D_\mathrm{O}N_\mathrm{O}^{(s)}}{\nu N_\mathrm{M}^{(o)}} \tag{3}$$

65 if

$$\frac{D_{\mathrm{M}}}{D_{\mathrm{O}}} \ll \frac{N_{\mathrm{O}}^{(s)}}{N_{\mathrm{M}}^{(o)}} \ll 1 \tag{4}$$

66 Alternatively,

$$k_{(n=2)} = \frac{2\pi}{D_{\mathrm{M}}} \left(\frac{D_{\mathrm{O}} N_{\mathrm{O}}^{(s)}}{2\nu N_{\mathrm{M}}^{(o)}} \right)^2 \tag{5}$$

67 if

$$\frac{N_{\mathrm{O}}^{(s)}}{N_{\mathrm{M}}^{(o)}} \ll \frac{D_{\mathrm{M}}}{D_{\mathrm{O}}} \ll 1 \tag{6}$$

68 Equations 3 and 5 provide a means of estimating precipitate penetration kinetics without the need for
69 experimental penetration data. However, Wagner's analysis relies on several critical assumptions [9, 14].
70 Three of these assumptions have been identified as having a high likelihood of being proved incorrect for real
71 systems [9]. The first assumption is that precipitates have high thermodynamic stability and will form at low
72 concentrations of both metal and oxidant. Where Equation 3 is applicable, this implies that the matrix
73 concentration of both components becomes negligible within the precipitation zone. However, where
74 diffusion of the metallic element is appreciable and Equation 5 applies, an accumulation of the metallic
75 element in the precipitation zone can occur. The second assumption is that the phase fraction of precipitates is
76 constant throughout the precipitation zone, changing discontinuously to zero at the precipitation front. The
77 third key assumption is that mass transfer occurs only by bulk diffusion in the matrix, and is unaffected by the
78 presence of second phases or interfaces.

79 These assumptions have been shown to be reasonable for some alloy-oxidant combinations. For example,
80 Young [9] demonstrated the success of Wagner's theory in predicting rate constants for oxidation of an
81 austenitic Ni-5Cr alloy at 1000 °C, and carburization of an austenitic Fe-20Ni-25Cr alloy, also at 1000 °C. In
82 both cases, the theoretical rate constant was within an order of magnitude of the experimentally measured rate
83 constant. In contrast, the predicted rate constant for nitridation of the same Fe-20Ni-25Cr alloy at 1000 °C
84 differed from the experimental rate constant by almost two orders of magnitude.

1.2 Nitridation of Fe-Ni-Cr alloys

A systematic evaluation of Wagner's assumptions for nitridation of Fe-Ni-Cr alloys does not appear to have been conducted. However, the literature indicates that formation of Cr_2N in Fe-Ni-Cr alloys is one of the cases where these assumptions break down [9]. Cr_2N has a relatively small standard free energy of formation in comparison to other nitrides [1], and appreciable chromium concentrations are required for precipitation to occur [9]. This suggests low thermodynamic stability. Furthermore, Udyavar and Young's study of Fe-Ni-Cr alloys nitrided at 1000 °C [15] showed that the volume fraction of Cr_2N in the precipitation zone was not constant. A strong dependence on distance from the free surface was evident. The same study also identified a higher Cr_2N penetration rate in samples with a higher volume fraction of precipitates. This implies that an increased volume fraction of Cr_2N will accelerate diffusion, disproving the assumption that mass transfer is unaffected by the presence of previously precipitated particles.

Chromium nitrides are known to form in Alloy 800H upon nitridation [16]. Hence a purely theoretical approach to determining nitridation kinetics is unlikely to prove accurate in the present study. In addition, Wagner's analysis has only been assessed for model Fe-Ni-Cr alloys. Formation of nitrides of the minor alloying elements often present in commercial alloys has not been examined. Aluminium nitride is also known to form in 800H [2, 16], but the current lack of solubility and diffusivity data for Fe-Ni-Cr-Al alloys means the applicability of Wagner's analysis has not yet been evaluated for this case. Determination of nitridation kinetics in the present study will therefore be reliant on experimental nitride penetration data.

Experimentally derived models [15–17] and some individual data points [18] for nitridation of 800H are available, but are limited to 1000 °C. Parabolic behavior was assumed *a priori*, which is common in studies of nitridation kinetics in Fe-Ni-Cr alloys (see e.g. [15, 17, 19–21]). However, cases of linear nitridation behavior have been reported in other alloys: Pint [22] observed linear nitridation kinetics in ferritic Fe-Al alloys upon addition of 5 wt% Cr, and Han and Young [7] noted that long-term nitridation behavior in Ni-Cr-Al alloys tended to be linear. Pint [22] suggested that linear kinetics were due to local volume changes as precipitates formed, causing damage to the matrix or surface scale and thereby allowing more rapid ingress of nitrogen.

Linear kinetics have also been experimentally observed where supply of the oxidant to the free surface is limited but oxidant diffusivity in the matrix is high, meaning oxidant supply becomes the rate-controlling factor [23]. Hence parabolic behavior cannot necessarily be assumed, and the temperature dependence of the reaction rate becomes uncertain. Extrapolating experimental observations at 1000 °C to service temperatures (approximately 850 °C for steam reformer applications [3,4]) given these unknowns is risky and has not been validated.

The present work is a study of nitride penetration kinetics for UNS N08810/Alloy 800H over a range of service-relevant temperatures (800 °C–1000 °C), where data was previously only available at 1000 °C. Phase stability, solubility limits and diffusivity data for nitridation of 800H are presented for the first time, and assumptions in Wagner's analysis of internal oxidation reactions are evaluated. The generalized kinetic model (Equation 1) is fitted to experimental data for AlN and Cr_2N penetration, where the exponent n is determined. These models are validated using separate experiments, and time-temperature-precipitation diagrams for AlN and Cr_2N penetration are determined.

2 Experimental Procedures

Alloy 800H in an annealed condition was studied. Specimens were in the form of seamless pipe with outside diameter 42.16 mm and wall thickness 6.35 mm (NPS 1-1/4" Sch. 160 [24]). All specimens were from the same original heat. Optical emission spectroscopy (OES) conducted with an Oxford Instruments Foundry-Master Xline was used to measure the composition of each as-received (AR) specimen used in this work. Two OES measurements were performed on each specimen. The variation in elemental composition between separate specimens was no greater than the variation of repeated measurements from any single specimen, hence all specimens were considered compositionally equivalent. The exact material composition is a proprietary formulation, but was verified to meet the specifications for 800H, given in Table 1. Similarly, the variation in grain size between specimens was no greater than the variation within a single specimen (see

Table 1 Specified composition of UNS N08810/Alloy 800H [wt%] [25]

Ni	Cr	Fe	C	Al	Ti	Al + Ti
30.0-35.0	19.0-23.0	39.5 min.	0.05-0.10	0.15-0.60	0.15-0.60	0.30-1.20

Supplementary Figure S1, refer to electronic supplementary material), hence specimens were also considered equivalent in this regard.

The nitridation treatment procedure was based on the requirements of ISO 21608: Test Method for Isothermal-Exposure Oxidation Testing under High-Temperature Corrosion Conditions for Metallic Materials [26]. Two AR specimens were cut into coupons with dimensions 15 mm × 12 mm × 4 mm, and ground to a 600 grit finish on all surfaces using SiC paper. Isothermal nitridation treatments were carried out in a Lindberg/Blue M 55000 series hinged tube furnace with a 95% N_2/5% H_2 atmosphere at 101.3 kPa (1 atm.). Coupon temperature was independently monitored throughout treatment using an Omega™ Super OMEGACLAD™ XL N-type thermocouple. To reduce oxygen partial pressure, titanium sponge was used as an oxygen getter, and the furnace tube was evacuated and backfilled with the test gas twice prior to beginning each treatment. Treatments were conducted for 50 h, 150 h, 350 h, and 750 h at each of 800 °C, 900 °C, and 1000 °C to give a total of 12 conditions. Times were selected based on the recommendations of ISO 21608 [26] to achieve even spacing on a log time scale. Duplicate coupons were used for each treatment.

Following nitridation, coupons were sectioned with a Buehler IsoMet® 11-1180 low-speed diamond saw, and mounted in Buehler ProbeMet™ mounting compound using a Buehler SimpliMet® 3000 automatic mounting press. Preparation for both optical and scanning electron microscopy (SEM) was carried out using a Buehler Beta automatic grinder-polisher with Vector® LC 250 power head. Samples were subjected to wet grinding with SiC paper to 600 grit, followed by diamond polishing to 3 µm on Buehler MasterTex™ pads, and a final polish with Buehler MasterMet™ 0.06 µm colloidal silica on a Buehler ChemoMet™ pad. No etchants were used.

Optical imaging was conducted using a Leica DM inverted research microscope with Nikon Digital Sight DS-Fi1 camera and Nikon NIS-Elements® F3.2 software. Backscatter imaging was carried out on a JEOL

JSM-7000F FEG-SEM. A JEOL JSM-IT300LV SEM with LaB_6 filament was used for electron backscattered diffraction (EBSD) and energy dispersive spectroscopy (EDS) analysis. Oxford Instruments HKL Nordlys III and X-Max™ 50 silicon drift detectors were used for EBSD and EDS, respectively, and were controlled via Oxford Instruments AZtecHKL software.

EBSD maps were used to determine grain size of AR and nitrided material. Maps were typically 2 mm^2 in area with a 5 µm step size. Maps with index rates less than 90 % were rejected. An automated circle intercept method implemented in MATLAB® R2017b [27] was used to calculate average grain diameter for each map. 5 maps were obtained for each coupon.

Combined EDS and EBSD point analysis was used for phase identification. Nitride penetration was measured from EDS maps. The Fiji distribution of ImageJ [28] was used for all measurements.

Thermo-Calc [29] with the TCFE8 Steels/Fe-alloys database was used for calculation of equilibrium phase fractions and compositions. Pressure was fixed at 101.3 kPa (1 atm.). The alloy composition used was the averaged composition of all AR specimens as measured using OES. The number of moles of all elements except nitrogen were fixed, with total system size a free variable to allow addition of nitrogen to the system without affecting the relative amounts of all other elements. Alloy nitrogen concentration was then varied using the single-axis calculation scheme, and equilibrium phase fractions and compositions were calculated at each step. Diffusivity of N, Al, and Cr in austenite with uniform composition was determined using Thermo-Calc and DICTRA [29], with the TCFE8 and MOBFE3 databases.

3 Results and Discussion

3.1 Microstructural characterization

The typical appearance of the as-received (AR) material is shown in Figure 1(a). The large precipitates visible in the austenite (γ) matrix were identified using EDS and EBSD as cubic Ti(C,N). N-rich precipitates appeared maize-colored and C-rich precipitates grey when viewed optically. This was consistent with the

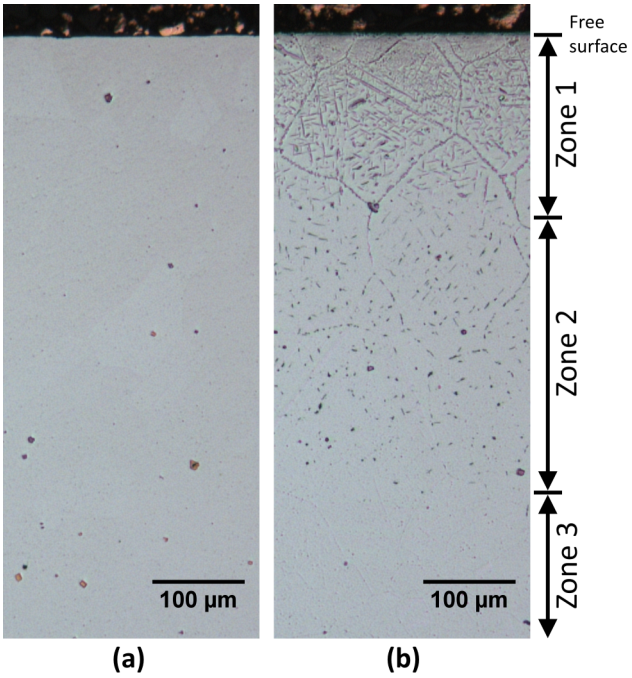

Fig. 1 Comparison of material appearance before and after nitridation. (a) As-received condition. Precipitates visible were Ti(C,N), which did not dissolve or change in appearance during nitridation treatment. (b) Following nitridation at 1000 °C for 50 h. Zone 1 corresponded to the region with Cr- and Al-rich nitrides, Zone 2 contained Al-rich nitrides, and Zone 3 was the remaining base material.

literature [30,31]. A uniform distribution of fine Ti-rich precipitates was also observed at high magnifications. Ti(C,N) is known to form in Alloy 800H during the manufacturing process [2,25].

The AR material had an equiaxed grain structure, with a log-normal size distribution and an average grain diameter of approximately 100 µm. Grain size can affect penetration kinetics of internal oxidation reactions, as grain boundaries are considered rapid diffusion paths and provide heterogeneous nucleation sites [9,23]. Hence any grain growth occurring during nitridation would be expected to reduce the rate of nitride penetration over time, due to reduction of the total grain boundary area. Beardsley *et al.*'s [32] work on homogenization of Alloy 800H tube after cold pilgering showed that a maximum grain size was attained after a one-hour heat treatment at all temperatures in the range 800 °C–1200 °C. This was attributed to pinning of grain boundaries by chromium carbides and Ti(C,N). The material used in the present study had been annealed post-forming, hence any further treatment-induced grain growth was considered unlikely. To confirm

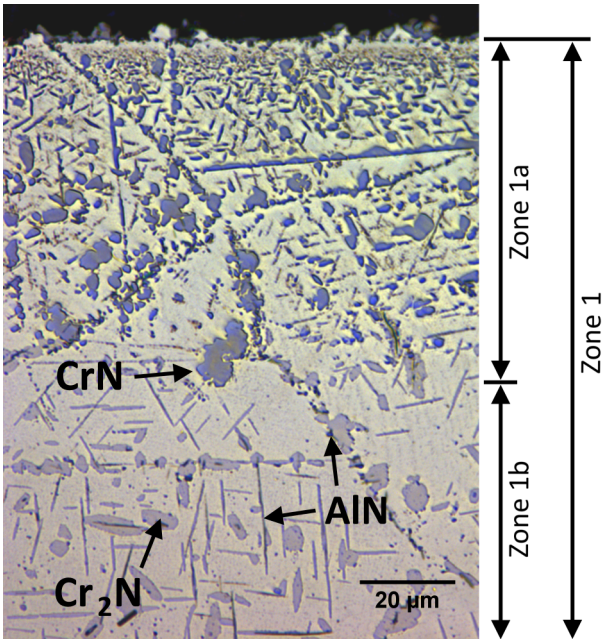

Fig. 2 Optical image showing CrN penetration, observed in coupons nitrided at 1000 °C for 750 h. Where CrN was present, Zone 1 was divided into Zone 1a, containing CrN (dark grey), Cr_2N (light grey), and AlN (black), and Zone 1b, containing Cr_2N and AlN.

this, the mean grain size of all nitrided coupons following treatment was compared, along with an untreated coupon from each original specimen of material. No systematic increase in mean grain size was observed for either increasing time or temperature (Supplementary Figure S2). Hence it was concluded that no grain growth had occurred.

Nitrided cross-sections showed a precipitation zone penetrating from the free surface inwards. Both grain boundary and intragranular precipitation was evident in all samples (Figure 1(b)). Precipitates were identified using EDS and EBSD as trigonal Cr_2N and hexagonal AlN. In samples nitrided at 1000 °C for 750 h, cubic CrN was also identified closest to the free surface (Figure 2). This is consistent with Welker *et al.*'s work on Alloy 800H [16], where CrN was only identified after nitriding at times exceeding 600 h at 1000 °C.

Ti(C,N) precipitates were present throughout all nitrided samples, but no precipitation front was observed. EDS mapping was used to compare the size and distribution of Ti-rich precipitates in the AR material with those in a sample nitrided at 1000 °C for 350 h. No clear differences in size distribution or number density of Ti(C,N) precipitates with area $\geq 2\,\mu m^2$ were observed between the two samples (Supplementary Figure S3).

The maximum cross-sectional area of the interaction volume for the EDS acquisition parameters used was calculated as $2\,\mu m^2$ [33]. This meant that precipitates with area smaller than this could not be reliably detected or measured using EDS. Characterization with transmission electron microscopy was beyond the scope of this work, hence changes in the size and/or distribution of the fine Ti(C,N) precipitates could not be quantified. Due to the lack of both a precipitation front and confirmation of any nitridation-induced changes, all Ti(C,N) precipitates were ignored in subsequent analysis.

Grain boundary Cr-rich $M_{23}C_6$ was present in all nitrided samples. It was identified using EDS and EBSD in all regions of the material, except where chromium nitrides were present. Co-existence with Cr_2N or CrN could not be confirmed. $M_{23}C_6$ is known to form in Alloy 800H upon aging at temperatures 540 °C–1095 °C [25, 34]. Hence it is likely that formation of $M_{23}C_6$ was a result of the treatment temperature and not the nitriding atmosphere. It was therefore ignored in subsequent analysis.

The nitrided microstructure was divided into zones according to nitride types (Figures 1 and 2). The region closest to the free surface was labeled Zone 1, consisting of $\gamma + \mathrm{AlN} + \mathrm{Cr_2N}$. Where CrN was present, Zone 1 was subdivided into Zone 1a ($\gamma + \mathrm{AlN} + \mathrm{Cr_2N} + \mathrm{CrN}$) and Zone 1b ($\gamma + \mathrm{AlN} + \mathrm{Cr_2N}$) (Figure 2). Zone 2 contained $\gamma +$ AlN, while Zone 3 was the remaining base material.

Nitride morphologies varied with location (high-angle grain boundary or intragranular) and distance from the free surface. Grain boundary AlN in Zone 1 had an acicular form, but Cr_2N had a blocky morphology (Figure 3(a)). Grain boundary precipitates typically have a mixture of coherent, semi-coherent, and incoherent interfaces with the differently-oriented matrix on either side of the boundary, leading to irregular morphologies [35]. Intragranular Cr_2N and AlN in Zone 1 typically had an acicular form. Three variants are visible in the upper grain of Figure 3(a). The orientation relationship between Cr_2N and austenite is documented as $\{111\}_\gamma \parallel \{0001\}_{\mathrm{Cr_2N}}$ and $\langle \bar{1}10 \rangle_\gamma \parallel \langle \bar{1}100 \rangle_{\mathrm{Cr_2N}}$ [36–38], and the same relationship has been observed for AlN [11]. This relationship means that formation of coherent or semi-coherent interfaces is possible, and hence is likely a strong determining factor for the shape and directionality of these intragranular precipitates [35].

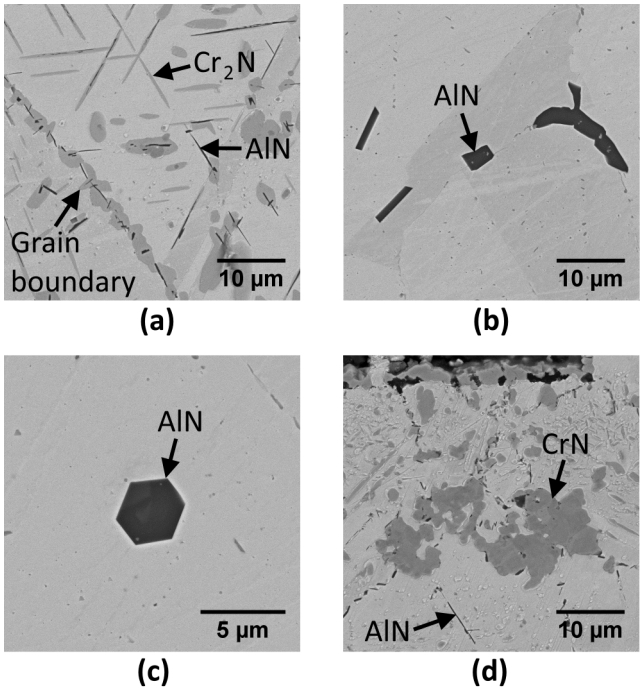

Fig. 3 Examples of typical nitride morphologies. Grey precipitates are Cr-rich. Black precipitates are Al-rich. (a) Cr_2N and AlN (Zone 1); (b) AlN (Zone 2); (c) Hexagonal AlN precipitate (Zone 2), a form not commonly observed in cross-section; (d) CrN (Zone 1a).

Close to the transition from Zone 1 to Zone 2 and throughout Zone 2, the morphology of AlN became more varied. Very few acicular precipitates were observed, with blocky and elongated, prismatic forms being more common (Figure 3(b)), as well as the occasional hexagonal section (Figure 3(c)). The different morphologies may reflect local compositional differences in the matrix, as a wide variety of AlN morphologies have been observed in steels depending on aluminium and nitrogen concentrations [11].

Where CrN appeared, it was present both on high-angle grain boundaries and intragranularly, but had no consistent form (Figure 3(d)). CrN has a face-centered cubic structure [31], so can obtain a cube-cube orientation relationship with the γ matrix. However, Tjokro and Young [17] observed transformation of trigonal Cr_2N to cubic CrN in commercial high-temperature alloys nitrided at 1000 °C–1200 °C. They stated that due to the difference in crystal structures of the two phases, the CrN-γ interface was unlikely to play a role in determining precipitate morphology. Hence any further growth of CrN would result in an irregular

form due to incoherent matrix-precipitate interfaces [17]. Furthermore, transformation of Cr_2N to CrN appears to be thermodynamically favorable. Ono-Nakazoto *et al.* [39] showed that formation of CrN from pure Cr_2N and N_2 gas resulted in a decrease in free energy of the system at temperatures 960 °C–1080 °C. In the present study, where CrN was identified it was the dominant precipitate in Zone 1a (Figure 2). The presence of Cr_2N could not be confirmed in this region through either optical or SEM methods. Hence it is likely that CrN is formed in 800H via transformation of Cr_2N to CrN.

EDS mapping was used to measure penetration of AlN and Cr_2N, as optical and backscatter imaging did not provide sufficient contrast between Cr- and Ti-rich phases. Al and Cr maps were obtained at 10 separate sites per coupon. With the free surface designated $x = 0$, the perpendicular distance to the point of deepest nitride penetration (x_{AlN} or $x_{\mathrm{Cr_2N}}$, as appropriate) was measured for each map (Figure 4(d)), according to ISO 26146: Method for Metallographic Examination of Samples after Exposure to High-Temperature Corrosive Environments [40]. Nitride penetration, x, increased with increasing treatment time, shown in the time series example in Figure 4. The mean penetration depth of each nitride type was calculated for each coupon (Figure 5). Coefficients of variation decreased with increasing temperature, and were in the range 1–8% for AlN, and 3–15% for Cr_2N. Through-thickness penetration of AlN occurred in 1000 °C–750 h coupons, hence $x_{\mathrm{AlN}} = 2000\,\mu\mathrm{m}$ was assumed.

CrN penetration in 1000 °C–750 h coupons was determined from optical images, due to an inability to distinguish CrN from Cr_2N using either EDS or backscatter imaging. Mean CrN penetration depth was $x_{\mathrm{CrN}} \approx 60\,\mu\mathrm{m}$. This is consistent with measurements by Welker *et al.* [16], where CrN penetration in Alloy 800H was less than 100 µm for times 650 h and 1000 h at 1000 °C.

Based on the experimentally observed precipitate penetration, the nitride precipitation sequence for this alloy was identified as $\gamma \rightarrow \gamma + \mathrm{AlN} \rightarrow \gamma + \mathrm{AlN} + \mathrm{Cr_2N} \rightarrow \gamma + \mathrm{AlN} + \mathrm{Cr_2N} + \mathrm{CrN}$. This was consistent with previous experimental observations for nitridation of Alloy 800H and its parent Alloy 800 in a N_2/H_2 atmosphere at 1000 °C [16, 17]. The precipitation sequence was also consistent with a phase diagram constructed from thermodynamic equilibrium calculations using Thermo-Calc [29] at temperatures 800 °C–1000 °C (Figure 6). Note that while the phase diagram gives the thermodynamically stable phases as a

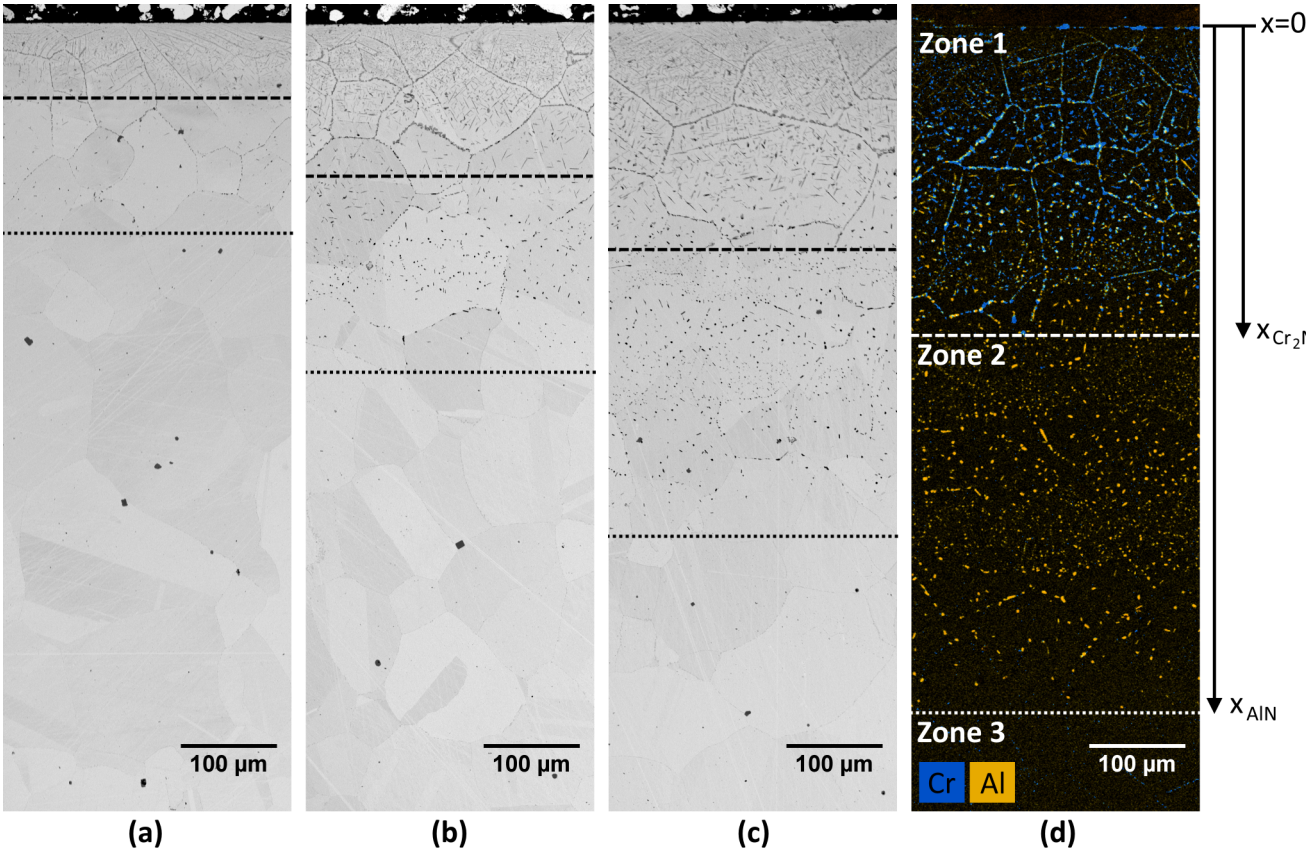

Fig. 4 Nitride penetration resulting from nitridation at 900 °C for (a) 50 h, (b) 150 h, (c) 350 h, and (d) 750 h. (a)-(c) are backscatter electron images (for illustrative purposes only), while (d) demonstrates penetration measurement methodology using overlaid EDS maps for Cr and Al. Dashed and dotted lines indicate approximate zone transitions. Cr_2N penetration, x_{Cr_2N}, was defined as the transition between Zones 1 and 2, and the transition from Zone 2 to Zone 3 marked AlN penetration, x_{AlN}.

function of increasing nitrogen in the base alloy, the actual precipitation sequence can be affected by kinetic effects such as nucleation barriers.

Other studies have made slightly different predictions of phase stability in Alloys 800H and 800HT (a more compositionally-restricted form of 800H). Erneman *et al.* [30] calculated equilibrium phase fractions as a function of temperature in Alloy 800HT. Thermo-Calc version R with the TCNI4 and TCFE3 databases was used. The reported nitrogen concentration corresponded to region B of Figure 6, but at temperatures 800 °C–1000 °C, Ti(C,N) was the only precipitate phase predicted to be stable. Similar calculations by Tan *et*

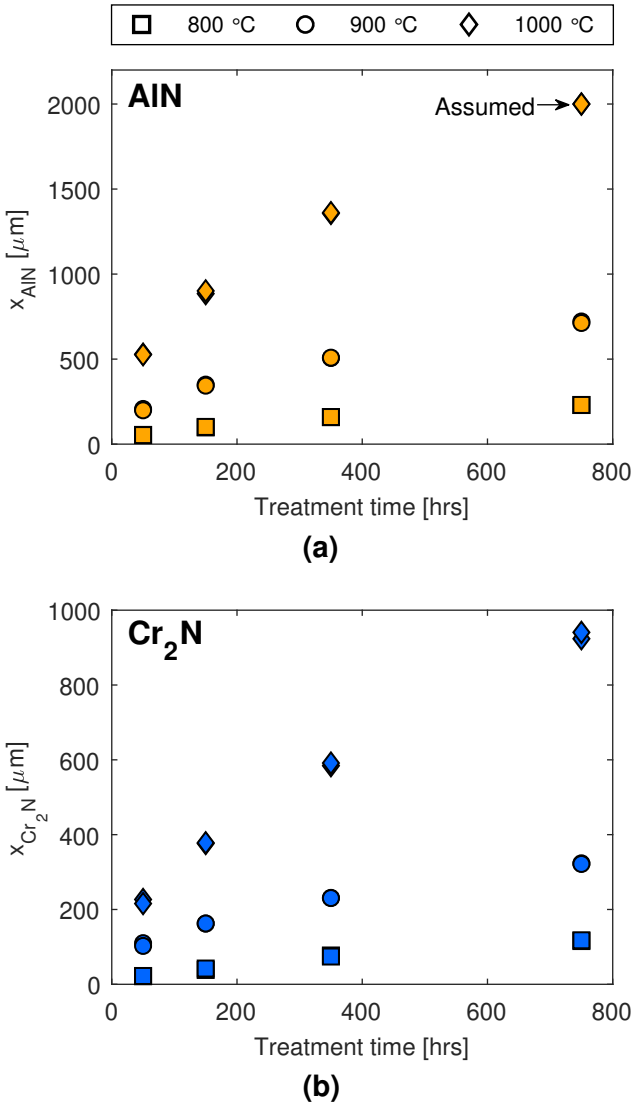

Fig. 5 Mean (a) AlN and (b) Cr_2N penetration in samples nitrided at 800 °C, 900 °C, and 1000 °C. The mean of 10 measurements from each coupon is shown, and two data points representing two sample coupons are plotted for each time. Coupons nitrided for 750 h at 1000 °C exhibited through-thickness AlN penetration.

al. [34] predicted that over the same temperature range, $Cr_{23}C_6$ and Ti(C,N) are the thermodynamically stable precipitate phases in Alloy 800H. Pandat and the PanFe database were used. The nitrogen concentration reported again corresponded to region B of Figure 6. $Ti_2(C,N)$ was also predicted to be stable at approximately 790 °C–925 °C, and $(Cr,Ti)_2(C,N)$ at approximately 975 °C–1200 °C.

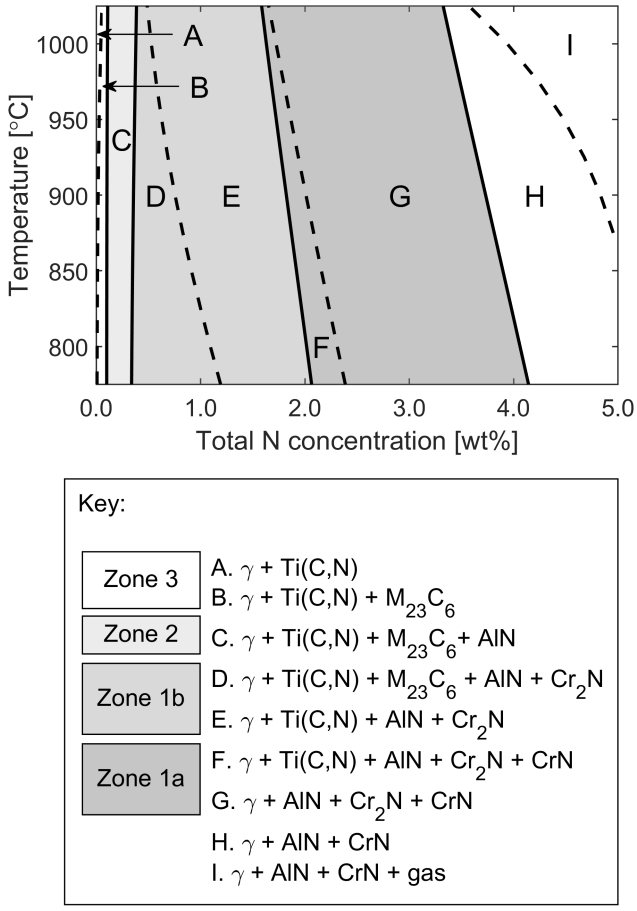

Fig. 6 Calculated phase diagram for Alloy 800H with changing total nitrogen concentration. OES-measured alloy composition was used. Solid lines indicate phase transitions where a nitride phase changes stability. Dashed lines indicate other solubility limits involving $M_{23}C_6$ or Ti(C,N). Hereafter, diagrams illustrating phase stability refer only to the nitride phases of interest, i.e. AlN, Cr_2N, and CrN.

The differences in predicted phase stability between the present study and the works of Erneman *et al.* [30] and Tan *et al.* [34] may be due to compositional differences affecting solubility limits. The compositions reported by these authors were most notably higher in Ti and Cr, and lower in Ni than the OES-measured composition used in the present study (cannot be stated for proprietary reasons). Nitrogen and carbon solubilities increase with decreasing Ni in Fe-Ni-Cr alloys [15]. Erneman *et al.* reported the lowest alloy Ni concentration, so a corresponding high carbon solubility may explain why $M_{23}C_6$ was not predicted to be

stable. Tan *et al.* reported the highest alloy Ti concentration, which may account for the predicted presence of the $Ti_2(C,N)$ and $(Cr,Ti)_2(C,N)$ phases. Furthermore, these studies also used different thermochemical models and databases that are likely to give slightly different predictions.

3.2 Evaluation of Internal Oxidation Theory

Wagner's analysis for internal oxidation [13] allows prediction of reaction kinetics without the need for experimental data, provided the underlying assumptions are satisfied. While the literature indicates that these assumptions will not be satisfied for formation of chromium nitrides in Alloy 800H [9, 15], the validity of Wagner's analysis for the case of AlN formation has not been assessed. Here the assumptions in the derivation of Equations 3 and 5 will be evaluated for AlN.

3.2.1 AlN

The first key assumption is that precipitates have high thermodynamic stability, and hence will form at low concentrations of both metal and oxidant [9, 14]. The standard free energy of formation of AlN is $-176\,\mathrm{kJ\,mol^{-1}}$ at 1000 °C [41]. This is one of the largest energies of formation of the common nitrides formed in engineering alloys [1]. Consequently, AlN is considered a high-stability phase in commercial high-temperature alloys [17]. Furthermore, Al concentration in 800H is low by necessity (< 0.6 wt%, see Table 1), and Figure 6 shows that AlN is stabilized at a total nitrogen concentration of approximately 0.1 wt%. Hence it can be concluded that AlN satisfies Wagner's assumption of high thermodynamic stability.

The second assumption is that the phase fraction of precipitates is constant in the precipitation zone [9]. Analysis of EDS maps for Al suggested that the area fraction of AlN remained approximately constant at around 4% throughout the nitridation zone in all nitrided samples. This is consistent with equilibrium calculations, which predicted the phase fraction of AlN to remain constant between a total nitrogen concentration of approximately 0.5 wt% and the calculation limit of 5 wt% at all experimental temperatures (Figure 7).

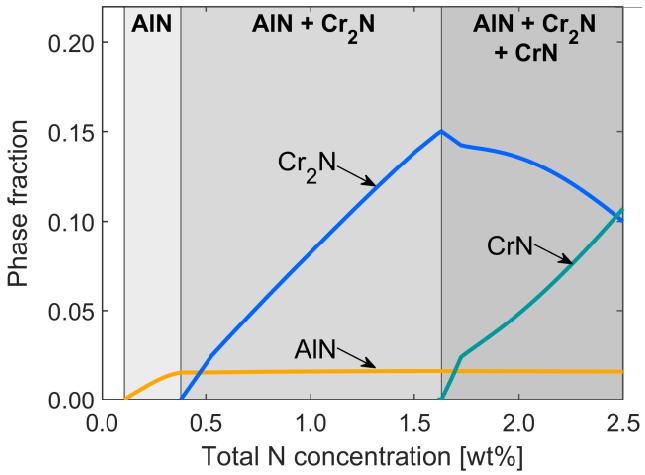

Fig. 7 Equilibrium phase fraction of nitride phases in Alloy 800H with increasing total nitrogen concentration at 1000 °C, calculated using Thermo-Calc [29]. OES-measured alloy composition was used. Phase fraction plots at 800 °C and 900 °C showed similar trends and are given in Supplementary Figure S4.

The third assumption that mass transfer is by bulk diffusion only and is unaffected by the presence of previously precipitated particles [9, 14] is more difficult to test. The uniformity of the precipitation front can give an indication of whether bulk or grain boundary diffusion is the dominant mechanism: a uniform front indicates that bulk diffusion dominates; advancement of the front along grain boundaries suggests that grain boundary diffusion is the more rapid mechanism of mass transfer [23]. In the present study, all AlN nitridation fronts were reasonably uniform, suggesting that grain boundary diffusion was not dominant (see Figure 4 for examples). Hence Wagner's assumption of bulk diffusion is likely to be valid. The effect on mass transfer of existing precipitates is commonly accounted for by including an empirical constant (also referred to as a "labyrinth factor"), ε, in Equation 3 [9]. This constant varies between 0 and 1, and effectively reduces the oxidant diffusivity. Its value is expected to be related to the phase fraction of precipitates, but due to the fact that this fraction is typically small, ε is usually assumed to be approximately 1 [9]. The phase fraction of AlN calculated in the present work was less than 2% at all experimental temperatures, hence the effect of newly formed AlN on mass transfer is likely to be negligible.

Table 2 Diffusivities of N, Cr, and Al in γ matrix at solubility limits for nitride formation, calculated using Thermo-Calc and DICTRA [29].

Phase transition	Element	D $[m^2 s^{-1}]$		
		800 °C	900 °C	1000 °C
$\gamma \rightarrow \gamma + AlN$	N	7.43e-13	3.32e-12	1.17e-11
	Al	1.18e-17	1.63e-16	1.50e-15
$\gamma + AlN \rightarrow \gamma + AlN + Cr_2N$	N	7.50e-13	3.37e-12	1.20e-11
	Cr	4.93e-18	7.29e-17	7.10e-16

Table 3 Solid solubility of nitrogen (mole fraction) in γ matrix for nitrogen activity of 0.95, calculated using Thermo-Calc [29].

$N_N^{(s)}$		
800 °C	900 °C	1000 °C
1.46e-4	2.85e-4	9.88e-4

Evidence from both experiment and thermodynamic calculations therefore indicates that Wagner's analysis is valid for the case of AlN formation in Alloy 800H. This means that it is possible to estimate the rate constant for parabolic precipitation kinetics without the need for experimental penetration data at the temperature of interest. Wagner [13] presents two limiting expressions for the rate constant (Equations 3 and 5), where selection of the appropriate form is dependent on the relative diffusivities and concentrations of the oxidant and the metallic element (Inequalities 4 and 6). Diffusivities of N and Al in the γ matrix were calculated for each experimental temperature at the solubility limit for the phase transition $\gamma \rightarrow \gamma + AlN$, using Thermo-Calc and DICTRA [29] (Table 2). Surface nitrogen activity was set to 0.95, corresponding to an ideal gas of 95% N_2/5% H_2. Nitrogen solid solubility ($N_N^{(s)}$) was assumed to be equal to the equilibrium matrix nitrogen concentration at a nitrogen activity of 0.95, and values were calculated for each experimental temperature (Table 3). $D_{Al}/D_N < 0.001$ and $N_N^{(s)}/N_{Al}^{(0)} \leq 0.1$ in this alloy at all experimental temperatures. Hence Inequality 4 is satisfied and Equation 3 is expected to apply for AlN penetration in Alloy 800H.

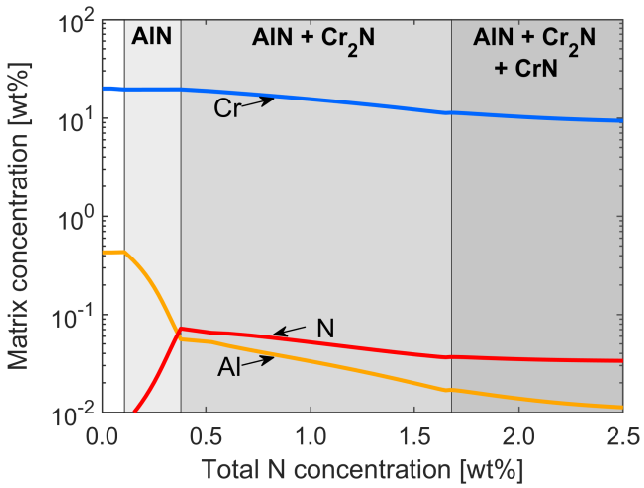

Fig. 8 Change in γ matrix composition with increasing total alloy nitrogen concentration at 1000 °C, calculated using Thermo-Calc [29] for alloy composition measured with OES. Composition plots at 800 °C and 900 °C showed similar trends and are given in Supplementary Figure S5.

Calculation of the equilibrium matrix nitrogen concentration as a function of total alloy nitrogen concentration further supports this. Where Equation 3 applies, matrix concentrations of the oxidant and metal are expected to become vanishingly small [9]. The concentrations of both Al and N were predicted to be negligible where AlN was thermodynamically stable (Figure 8). EDS point measurements in the precipitation zone indicated that matrix Al concentration was too low to be reliably measured (< 0.2 wt%). Nitrogen cannot be accurately quantified using EDS.

Theoretical rate constants calculated using Equation 3 (denoted $k_{(n=2),th}$) are given in Table 4. A graphical comparison of the theoretical models to measured AlN penetration is provided in Figure 9. Agreement between the theoretical models and experimental data was good at 800 °C and 900 °C. The model at 1000 °C overestimated AlN penetration, but the 750 h data point is a lower bound. This suggests a lower nitrogen diffusivity than that given in Table 2.

Table 4 Theoretical rate constants for AlN penetration calculated from Equation 3, assuming parabolic kinetics.

$k_{(n=2),th}$ [$m^2\,s^{-1}$]		
800 °C	900 °C	1000 °C
2.48e-14	2.16e-13	2.64e-12

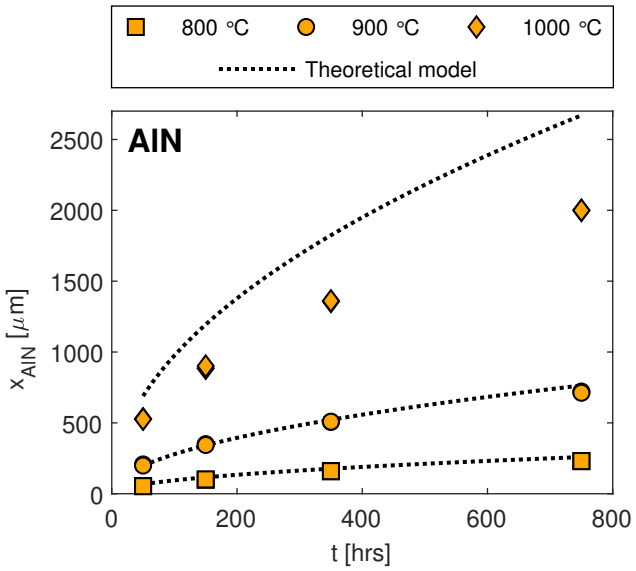

Fig. 9 Comparison of theoretical kinetic models calculated from Equation 3 to measured AlN penetration. Each data point is the mean of 10 measurements per coupon. There are two data points per treatment condition. Values of $k_{(n=2),th}$ are given in Table 4.

3.2.2 Cr_2N

The present study confirms that precipitation of chromium nitrides in Alloy 800H does not conform to Wagner's analysis. First, the standard free energy of formation of Cr_2N is low ($-31\,kJ\,mol^{-1}$ at 1000 °C [41]), indicating low thermodynamic stability. Furthermore, Cr_2N does not form at low concentrations of Cr and N. 800H contains around 20 wt% Cr, but Cr_2N does not form until the total alloy nitrogen concentration reaches approximately 0.4 wt% (Figure 6).

Secondly, the fraction of chromium nitrides varied throughout the precipitation zone, contradicting the assumption of constant phase fraction. Analysis of EDS maps for Cr indicated that the area fraction of

chromium nitrides decreased with increasing distance from the free surface (corresponding to decreasing nitrogen concentration). Equilibrium calculations predicted that phase fraction of both Cr_2N and CrN would increase with increasing nitrogen concentration (Figure 7). However, where stabilization of CrN was predicted, Cr_2N fraction decreased as CrN fraction increased. This is likely a consequence of the probable transformation of Cr_2N to CrN, as discussed in Section 3.1.

The Cr_2N precipitation front was again reasonably uniform, suggesting that Wagner's third key assumption may be valid for Cr_2N penetration. However, the calculated maximum phase fraction of Cr_2N approaches 20% (Figure 7), so it is unlikely that mass transfer will be unaffected by these precipitates.

From Tables 2 and 3, $D_{Cr}/D_N < 0.0001$ and $N_N^{(s)}/N_{Cr}^{(o)} < 0.005$ at all experimental temperatures. Hence Inequality 4 is satisfied, indicating Equation 3 is the limiting case best representing penetration of chromium nitrides. However, this implies that the matrix concentrations of metal and oxidant within the precipitation zone should be vanishingly small [9, 14]. EDS measurements of the matrix concentration of Cr within the precipitation zone showed that it did not drop below 8 wt% in any sample, and hence could not be considered negligible. This was supported by equilibrium calculations of the matrix composition at each experimental temperature (Figure 8).

The inability to apply Wagner's analysis means that estimation of rate constants for penetration of chromium nitrides is not straightforward in the absence of experimental data. A further complicating factor is the formation of multiple nitride types in Alloy 800H. Attempts to analytically predict penetration of the less stable precipitate in cases of oxidation of two solute metals have not met with great success [9]. Numerical modeling of the nitridation process may offer some insight into the rate-controlling factors.

3.3 Nitridation Kinetics

The demonstrated validity of Wagner's analysis for AlN penetration in Alloy 800H indicates a diffusion-controlled reaction following Equation 2. However, Wagner's assumptions do not hold for Cr_2N penetration, indicating Equation 2 should not be applied for Cr_2N. As validation, Equation 1 was fitted to the

Table 5 Fitted model parameters for nitride penetration, using a general kinetic model $x^n = kt$.

Nitride type	Temperature [°C]	n [-]	k [$m^n s^{-1}$]
AlN	800	1.85	7.01e-14
	900	2.15	6.59e-14
	1000	2.06	9.96e-13
Cr_2N	800	1.59	2.07e-13
	900	2.44	1.07e-15
	1000	1.89	6.43e-13

mean penetration data for AlN and Cr_2N at each temperature. Data was log-transformed to allow the parameters n and k to be determined using linear least-squares regression. The fitted parameters for all temperatures are given in Table 5, and comparison to experimental data points is illustrated in Figure 10. $R^2 > 0.99$ for all models. 95% confidence intervals were also calculated on the values of n and k for each model. The numerical values of these intervals are given along with illustrations of the fitted confidence intervals for all experimental temperatures in Supplementary Figures S6 and S7.

3.3.1 AlN

Values of n were ≈ 2 for all AlN penetration models (Table 5). This indicates close approximation of parabolic behavior, consistent with a diffusion-controlled reaction. As further confirmation, parabolic kinetics were assumed and models were re-fitted according to Equation 2. Graphical and numerical comparisons of the general and parabolic models are provided in Supplementary Figure S8 and Supplementary Table S1, respectively, and agreement between the two was good for AlN. $R^2 > 0.98$ for all parabolic models for AlN penetration, compared to $R^2 > 0.99$ for all general models. Model equivalence was further evaluated through comparison of model and experimental errors, due to the small number of data points used to fit each model. Two data points per treatment condition were used for model fitting, and the average difference between these two points was calculated for each model. The maximum value across all models was 4%. The normalized

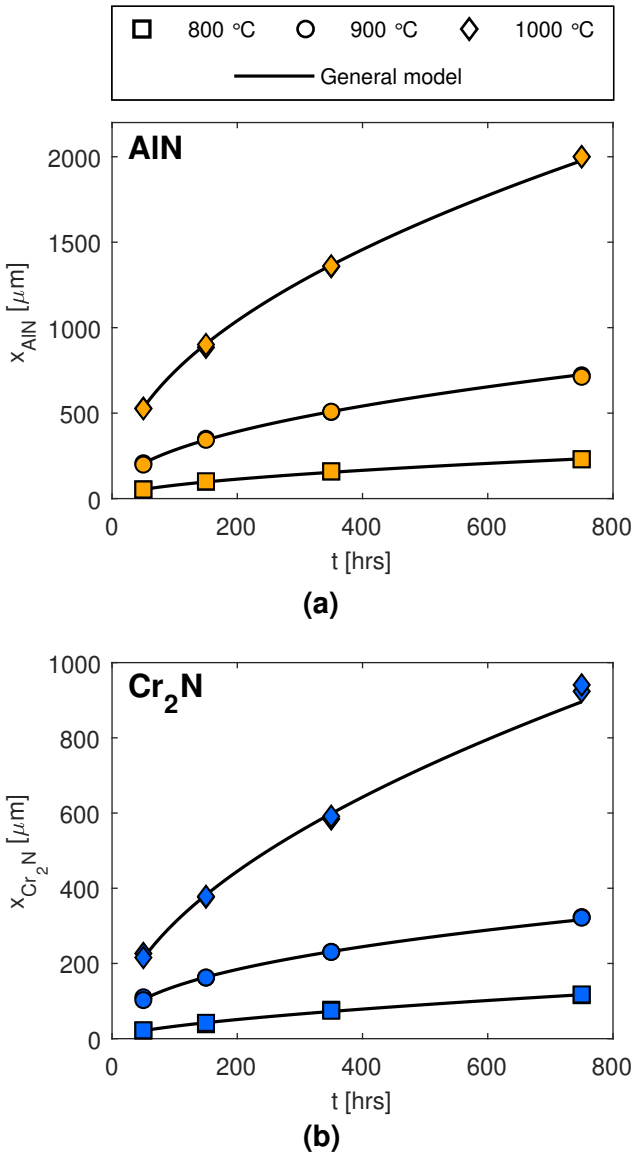

Fig. 10 Illustration of general kinetic models ($x^n = kt$) fitted to (a) AlN and (b) Cr_2N penetration measurements. Each data point is the mean of 10 measurements per coupon. There are two data points per treatment condition. Values of n and k are given in Table 5.

root mean square error (NRMSE, normalized by the mean of the data points used for fitting each model) of all general and parabolic AlN models was $< 4\%$ at all temperatures. Hence for AlN, the experimental error is greater than the model error for both model types, and either can be considered a good representation of the experimental data.

While both the experimentally determined general and parabolic models provide an accurate description of AlN penetration kinetics, the general model can only be applied at the experimental temperatures used in this study. Variation in the value of n means that the units of k are not consistent. Hence an Arrhenius analysis to determine the temperature dependence of k is not possible. However, the parabolic model has a fixed value of n, meaning predictions can be made at other temperatures. The temperature dependence of $k_{(n=2)}$ was determined from Equation 7,

$$k_{(n=2)} = k_0 \exp(\frac{-Q_{pen}}{RT}) \tag{7}$$

where k_0 is the pre-exponential coefficient, and Q_{pen} is the activation energy for nitride penetration. The experimental values of k_0 and Q_{pen} for AlN were calculated as $0.0159\,\mathrm{m^2\,s^{-1}}$ and $245\,\mathrm{kJ\,mol^{-1}}$, respectively. According to Equation 3, the theoretical activation energy for the rate constant is given by Equation 8,

$$Q_{pen} = Q_{dif} + Q_{sol} \tag{8}$$

where Q_{dif} and Q_{sol} are the activation energies for nitrogen diffusivity and solubility, respectively. Q_{dif} was calculated from the diffusivity data in Table 2 according to Equation 9,

$$D = D_0 \exp(\frac{-Q_{dif}}{RT}) \tag{9}$$

where D_0 is the diffusion coefficient. At the nitrogen solubility limit for the phase transition $\gamma \rightarrow \gamma + \mathrm{AlN}$, $Q_{dif} = 157\,\mathrm{kJ\,mol^{-1}}$.

It has previously been assumed that nitrogen solubility in alloys similar to 800H is reasonably insensitive to temperature around 1000 °C and therefore does not contribute to the penetration activation energy (see e.g. [9, 42,43]). In the present study, temperature dependence of nitrogen solubility was determined using the solubility data in Table 3 and Equation 10,

$$N_{\mathrm{N}}^{(s)} = N_0 \exp(\frac{-Q_{sol}}{RT}) \tag{10}$$

where N_0 is the solubility coefficient. Q_{sol} was calculated as $107\,\mathrm{kJ\,mol^{-1}}$. This indicates that nitrogen solubility cannot be considered insensitive to temperature for this alloy, and hence will contribute to the activation energy for nitride penetration.

From Equation 8, the theoretical rate constant activation energy for AlN is predicted to be 264 kJ mol^{-1}, which agrees well with the experimental activation energy for parabolic AlN penetration of 245 kJ mol^{-1}. This implies that Equation 3 will predict AlN penetration with reasonable accuracy at temperatures beyond those considered in the present study. Extension to other Fe-Ni-Cr-Al alloy systems is also likely to prove successful, provided Wagner's assumptions are satisfied for these other systems. However, experimental validation is still required.

3.3.2 Cr_2N

Cr_2N penetration did not demonstrate the same similarity to parabolic behavior as AlN penetration. Values of n for Cr_2N deviated from 2 by up to 22% (Table 5). Comparison of general and parabolic models fitted to experimental data indicated that the general model was a better representation of Cr_2N penetration (Supplementary Figure S8 and Supplementary Table S1). The NRMSE of the general model was less than the experimental error threshold of 4% at all temperatures, while that of the parabolic model ranged from 5% at 1000 °C to 12% at 800 °C. Hence the general model was considered the more accurate representation, and was subsequently used in all further analysis of Cr_2N penetration.

A validation experiment was conducted, where seven samples were nitrided at 1000 °C for 800 h. The treatment was designed such that prediction of Cr_2N penetration required the general model to be extrapolated to a time not yet studied in this work. 95% prediction intervals on the predicted mean penetration were calculated to aid in assessing prediction accuracy. A prediction interval is wider than a confidence interval, as it accounts for the additional error introduced by the fact that predictions are made using an estimated model response. A confidence interval describes the true mean model response based on a specific set of observations. Future observations are independent of the data used to fit the model, so a confidence interval cannot account for the additional error associated with these new observations. A comprehensive description of confidence and prediction intervals and their calculation can be found in Montgomery and Runger [44].

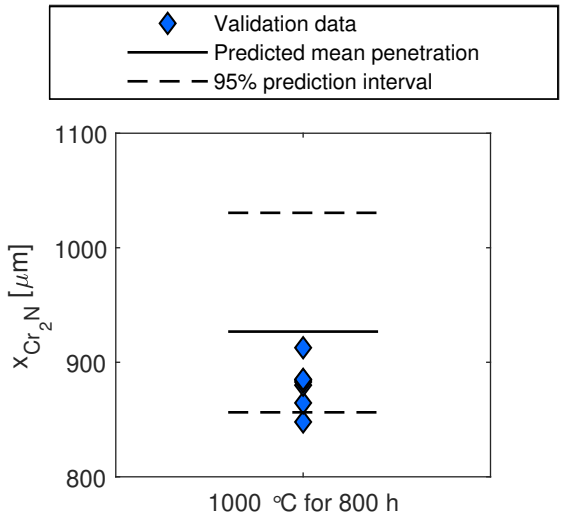

Fig. 11 Experimental validation of prediction capabilities of general model for Cr_2N. Validation samples were nitrided at 1000 °C for 800 h. 6 out of 7 samples fell within the general model 95% prediction interval.

Measured mean Cr_2N penetration was in the range 848 µm–913 µm. Six of the seven samples fell within the 95% prediction interval of $x_{Cr_2N} = 856$ µm–1034 µm given by the general model (Figure 11). The general model was therefore considered valid.

The success of the general model in predicting Cr_2N penetration raises a number of important considerations. First, non-parabolic kinetics may imply that diffusion of nitrogen is not the rate-controlling factor for Cr_2N penetration. Second, it means that the ability to model Cr_2N penetration is limited to the experimental temperatures studied. Third, it highlights the need for caution in extrapolation of existing models. In this work, it was noted that all validation data points fell below the extrapolated model mean (Figure 11). This implies that due to the model only being fitted to data from times up to 750 h, the effect of some phenomenon only occurring at longer times was not correctly captured. For example, the probable transformation of Cr_2N to CrN may affect Cr_2N penetration kinetics, but due to a lack of experimental data any such effect is currently unknown.

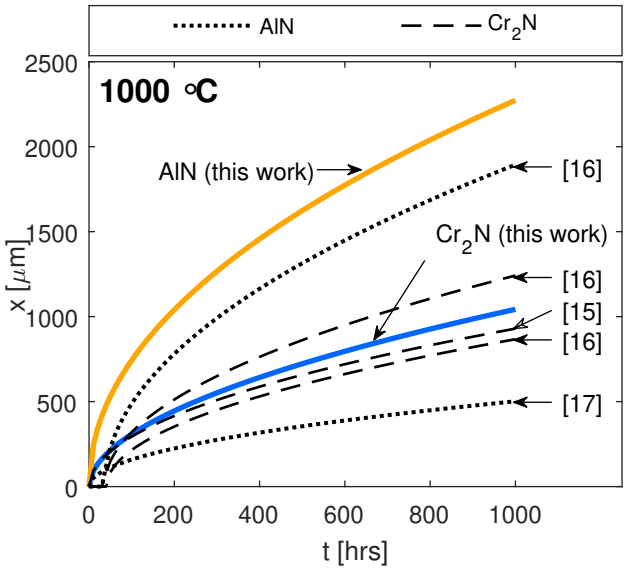

Fig. 12 Comparison of general models developed in this work (indicated) to models from the literature for nitridation at 1000 °C. Experimentally determined models for 800H-type alloys nitrided in a 95% N_2/5% H_2 atmosphere [16,17], and a Fe-15Cr-21.5Ni alloy nitrided in a 90% N_2/10% H_2 atmosphere [15] are shown.

3.3.3 Comparison to literature

Previous studies on Fe-Ni-Cr alloys have focused on nitridation at 1000 °C. Cr_2N kinetics determined in the present study were consistent with experimentally determined models for Alloy 800H nitrided in a 95% N_2/5% H_2 atmosphere [16], and a Fe-15Cr-21.5Ni alloy nitrided in a 90% N_2/10% H_2 atmosphere [15], both at 1000 °C (Figure 12). The AlN penetration kinetics determined in this work were also similar to Welker *et al.*'s [16] experimentally determined model for Alloy 800H nitrided in a 95% N_2/5% H_2 atmosphere at 1000 °C. However, Tjokro and Young's [17] experimental model for AlN in Alloy 800 nitrided under the same conditions showed much slower kinetics than the present study. The Al concentration in the alloy studied by Tjokro and Young was lower than that of the 800H used in the present study, which may account for the difference in nitridation rates. Furthermore, Tjokro and Young's maximum nitridation time was only 30 h, so extrapolation of their model to long times as shown in Figure 12 may be inaccurate.

The kinetics determined in this work predict greater penetration than Welker *et al.*'s [16] parabolic models for the same nitrides in Alloy 800H (Figure 12). Welker *et al.* determined parabolic rate constants for AlN of

460 1.03×10^{-12} m^2 s^{-1} and Cr_2N of 2.18×10^{-13} m^2 s^{-1} at 1000 °C. The parabolic rate constants determined in
461 the present work were 1.47×10^{-12} m^2 s^{-1} for AlN and 3.12×10^{-13} m^2 s^{-1} for Cr_2N at 1000 °C
462 (Supplementary Table S1). However, Welker *et al.* also found that when Al was removed from Alloy 800H,
463 Cr_2N was the only nitride to form in the resulting alloy, and the parabolic rate constant for Cr_2N penetration
464 increased to 4.44×10^{-13} m^2 s^{-1} (Figure 12).

465 The most notable difference between the present study and that of Welker *et al.* [16] was that those models
466 included an incubation time of approximately 40 h during which no nitride formation occurred. This
467 incubation time was attributed to a thin external oxide layer forming as a result of the test gas not being
468 completely oxygen-free. Welker *et al.* also reported a grain size of 60 µm–90 µm (distribution unknown), in
469 comparison to approximately 100 µm for the material used in the present study.

470 The incubation time does not account for the difference in penetration at long times, but the presence of an
471 oxide layer may contribute to the lower reaction rates in comparison to the present work. Zheng and Young
472 [45] suggested that nitrogen is transferred through a Cr_2O_3 surface scale by means of imperfections in the
473 scale such as cracks and pores. Hence the rate of nitrogen uptake, and therefore the rate of precipitate
474 penetration, depends on the condition of the surface scale. The Al concentration in Welker *et al.*'s [16] alloy
475 was lower than in the present study, which may also have contributed to the lower AlN penetration rate. The
476 smaller grain size reported by Welker *et al.* would only be expected to have an effect on penetration kinetics if
477 the rate of grain boundary diffusion was greater than that of lattice diffusion [9, 23]. A hallmark of this is
478 advancement of precipitation at grain boundaries. However, nitridation fronts at 1000 °C in both this work and
479 that of Welker *et al.* were reasonably uniform, indicating similar lattice and grain boundary diffusion rates.
480 Hence it is unlikely that grain size had a significant effect on penetration rate.

481 3.4 Time-Temperature-Precipitation Diagrams

482 The general model constants from Table 5 were used to construct time-temperature-precipitation (TTP)
483 diagrams for AlN and Cr_2N penetration in 800H (Figure 13). 95% prediction intervals calculated for each

model were used to determine error bars indicating the expected variation in time required to achieve a specified penetration depth. For example, the predicted mean time to achieve AlN penetration to 3000 µm (approximately the half-thickness of a commercial pigtail tube) at a temperature of 1000 °C is 1800 h, but the predicted interval within which this penetration depth may be achieved is 1660 h–1950 h (Figure 13(a)). For AlN, iso-penetration contours were also calculated from the Arrhenius analysis of the experimentally determined parabolic rate constants (Section 3.2).

Figure 13(a) shows that predicted AlN penetration consistently demonstrates more rapid kinetics as temperature increases. Equilibrium calculations using Thermo-Calc [29] indicate that AlN is stable up to the alloy melting temperature of approximately 1350 °C. The parabolic model predicts a continual increase in reaction rate with increasing temperature, but further experimental work is required to validate extrapolation of the model to the melting temperature. Equally, extension to low temperatures should also be treated with some caution, due to the likelihood of interfacial diffusion being favored over bulk diffusion at low temperatures [35]. However, agreement between predictions from the general and parabolic models was good for the temperatures illustrated in Figure 13(a), indicating that interpolation of the parabolic models for AlN to other temperatures is reasonable.

Figure 13(b) shows the predicted Cr_2N penetration during nitridation based on the general model. If the inverse of the time to obtain a certain precipitate penetration depth x_0 is the rate r_{x_0} of precipitate penetration, then $r_{100\,\mu m}$ and $r_{500\,\mu m}$ are each increasing functions of temperature. This does not hold for $r_{3000\,\mu m}$. Acknowledging the Cr_2N precipitation during nitridation in 800H does not accord with the assumptions in Wagner's oxidation theory (Section 3.2.2) nor does it display parabolic kinetics (Section 3.3.2), there is no reason to expect that all rates of penetration should be necessarily higher at higher temperature. The well-known C-shaped curves obtained for diffusional transformations in isothermal time-temperature-transformation diagrams illustrate the competition between nucleation and growth at various temperatures [46]. The rates of transformation do not increase monotonically with temperature where diffusional mass transport and nucleation are both important. Nucleation can play an important role in precipitation of relatively low stability phases such as Cr_2N [9].

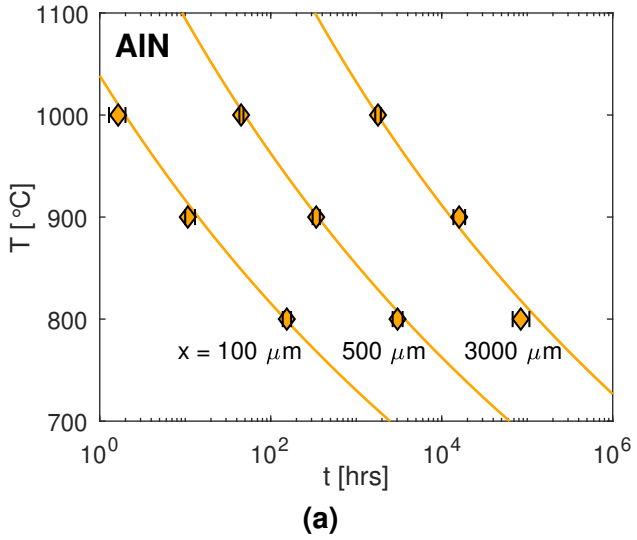

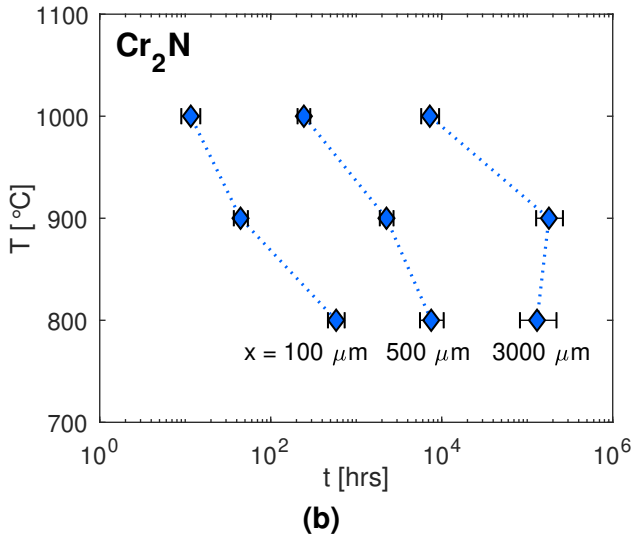

Fig. 13 Time-temperature-precipitation diagrams showing penetration depth (x) of (a) AlN and (b) Cr_2N in UNS N08810/Alloy 800H. Diagrams are for a mean grain size of approximately 100 µm, and a nitriding atmosphere of 95% N_2/5% H_2 at 101.3 kPa (1 atm.). Symbols represent predictions from the general kinetic models (Table 5). Error bars indicate 95% prediction interval on mean time taken to achieve specified nitride penetration depth. Contours in (a) were calculated from Arrhenius analysis of the fitted parabolic rate constants (Supplementary Table S1) according to Equation 7. Dotted lines in (b) are to guide the eye only.

Further, the predictions for $r_{3000\,\mu m}$ are based on extrapolation of the general model at each temperature. An inference from the validation experiment conducted at 1000 °C for 800 h (Figure 11) is that the fitted model may overestimate the Cr_2N penetration at times greater than 750 h, the longest heat treatment time for fitting the data set in this study. This could be due to the competition between CrN and Cr_2N near the free surface at longer times. In the fitting data, CrN was only identified in the sample nitrided at the highest temperature for the longest time, 1000 °C and 750 h. This is consistent with the equilibrium phase relations where the CrN solvus (boundary between regions E and F in Figure 6) moves to higher nitrogen concentration as temperature decreases. This means that the effect of CrN precipitation on the Cr_2N penetration kinetics is not included in the general model fits at 900 °C and 800 °C. Hence while the TTP diagram for Cr_2N shows the model prediction for the time to obtain precipitate penetration to 3000 µm, these should not be used without further validation.

It is important to note that these TTP diagrams are for simple nitriding conditions where $a_{N_2} = 0.95$ at the free surface. This is not representative of typical service atmospheres for this type of alloy, which is most often used in air ($a_{N_2} \approx 0.78$). However, internal nitridation has been observed in Fe-Ni-Cr and Ni-based alloys aged in air (see e.g. [19,22,20,47]). Data specific to 800H is scarce, although Erneman *et al.* [30] observed sparse AlN through the thickness of a 5 mm–diameter specimen of Alloy 800HT during creep testing to rupture in air at 1000 °C. Harper *et al.* [48] also identified acicular Cr-rich nitrides and AlN beneath a Cr-rich oxide scale in Alloy 800HT aged in air at 980 °C for 720 days. In general, nitride penetration depths reported in the literature for Fe-Ni-Cr and Ni-based alloys aged in air were much smaller than those observed in this study. For example, Elger and Pettersson [19] observed AlN to a depth of 70 µm beneath a mixed-oxide scale in a Fe-20Cr-25Ni stainless steel after 100 h in air at 1000 °C. The present study predicts AlN penetration of 740 µm for the same time and temperature in a N_2 atmosphere. The much slower nitridation kinetics demonstrated in air are likely due to oxide formation being thermodynamically favored over nitride formation [1], and the lower nitrogen activity.

There may exist specific cases where the kinetics determined in this work are applicable to air atmospheres. Welker *et al.* [16] found that in 800H, conditions at a growing creep crack in air evolved such that local

oxygen concentration was sufficiently depleted for internal nitridation to occur. Nitride penetration kinetics at the creep crack faces were quantitatively similar to those determined for unstressed aging of the same material under nitriding conditions, which were in turn similar to the kinetics determined in the present study (see Figure 12 for comparison). This implies that with further knowledge of the effects of internal nitridation on creep and fracture behavior of 800H, the present study can be used to assess the rate of material and property degradation during service.

4 Summary and Conclusions

The internal nitridation behavior of a UNS N08810/800H alloy with approximate grain size 100 µm in a N_2/H_2 atmosphere was studied at temperatures 800 °C–1000 °C for a series of times up to 750 h. The as-received material consisted of an austenite matrix with dispersed Ti(C,N). Nitridation resulted in both grain boundary and intragranular AlN, Cr_2N, and, at long times at 1000 °C, CrN. A phase diagram for 800H giving phase stability as a function of nitrogen concentration, calculated using Thermo-Calc, was presented for the first time. The experimentally observed precipitation sequence was consistent with the phase diagram. Measured AlN penetration ranged from approximately 50 µm after 50 h at 800 °C, to through-thickness penetration in the 4 mm-thick samples after 750 h at 1000 °C. Cr_2N penetration ranged from 20 µm to 940 µm for the same conditions. In the 1000 °C–750 h samples where it appeared, CrN penetration was approximately 60 µm.

The applicability of Wagner's theory of internal oxidation was evaluated for AlN and Cr_2N penetration. Equilibrium calculations of nitrogen solubility, nitride phase fractions, and alloy matrix composition as a function of nitrogen concentration showed that Wagner's analysis for internal oxidation was valid for AlN penetration. Previously unavailable diffusivity data for 800H was also calculated using Thermo-Calc and DICTRA, and theoretical rate constants for AlN penetration were determined.

Cr_2N penetration did not conform to Wagner's analysis, requiring kinetics to be determined from experimental data. Models were previously only available at 1000 °C for 800H. Penetration kinetics for both

AlN and Cr_2N at each experimental temperature were determined using a general model of the form $x^n = kt$. AlN penetration showed a close approximation of parabolic behavior. Evaluation of activation energies for nitrogen diffusion and AlN penetration showed that bulk nitrogen diffusion was the primary rate-controlling factor for AlN penetration.

Values of n for Cr_2N deviated from the ideal value of 2 by up to 22%. This deviation from parabolic kinetics suggested other rate-controlling factors besides diffusion. Hence prediction capabilities were limited to the experimental temperatures. A separate sample treatment designed to test extrapolation at 1000 °C successfully validated the predictive capabilities of the general models.

Time-temperature-precipitation diagrams illustrating AlN and Cr_2N penetration for this alloy were constructed from the kinetic models. Statistical analysis provided a means of estimating error when using the TTP relations as a prediction tool.

The nitridation behavior of this alloy indicates that AlN formation is most important when considering the effects of nitride penetration. The present study gives an accurate description of the kinetics of AlN penetration for a range of service-relevant temperatures for UNS N08810/Alloy 800H. The close approximation of parabolic kinetics demonstrated shows potential for extension to other temperatures with minimal loss of accuracy. Furthermore, estimation of AlN penetration rates for other Fe-Ni-Cr-Al alloy systems using Wagner's kinetic analysis may also be feasible, provided the appropriate diffusivity and solubility data is available.

Acknowledgements The financial support of the Methanex Corporation in conducting this research is gratefully acknowledged. The authors would like to thank Peter Tait of Methanex New Zealand Ltd. for his support, and Assoc. Prof. Matt Watson and Leigh Richardson from the University of Canterbury Chemical and Process Engineering Department for the use of their facilities and their assistance in conducting nitridation treatments.

References

1. G. Y. Lai: *High-Temperature Corrosion and Materials Applications*, 1st ed., ASM International, Materials Park, OH, 2007.

2. C. W. Thomas and M. J. Smillie: in *Ammonia Technical Manual*, vol. 52, American Institute of Chemical Engineers, Montreal, CA, 2011, pp. 101–111.
3. P. Kodali and J. P. Richert: in *Corrosion 2003*, NACE International, Houston, TX, 2003.
4. J. J. Hoffman and G. Y. Lai: in *Corrosion 2005*, NACE International, Houston, TX, 2005.
5. S. N. Monteiro: in *Corrosion in the Petrochemical Industry*, 1st ed., ASM International, Materials Park, OH, 1994, pp. 351–354.
6. M. Ashby and B. Dyson: in *Fracture 84*, Pergamon Press, New Dehli, India, 1984, pp. 3–30.
7. S. Han and D. J. Young: *Oxid. Met.*, 2001, vol. 55, pp. 223–242.
8. V. B. Trindade, U. Krupp, B. Gorr, D. Kaczorowski, G. Girardin, and H. J. Christ: *Mater. Corros.*, 2008, vol. 59, pp. 602–608.
9. D. J. Young: *High Temperature Oxidation and Corrosion of Metals*, 1st ed., Elsevier, Oxford, UK, 2008.
10. R. Elger, H. Magnusson, and K. Frisk: *Mater. Corros.*, 2017, vol. 68, pp. 143–150.
11. F. Wilson and T. Gladman: *Int. Mater. Rev.*, 1988, vol. 33, pp. 221–288.
12. J. W. Simmons: *Metall. Mater. Trans. A*, 1995, vol. 26, pp. 2579–2595.
13. C. Wagner: *Z. Elektrochem.*, 1959, vol. 63, pp. 772–782.
14. R. A. Rapp: *Corrosion*, 1965, vol. 21, pp. 382–401.
15. M. Udyavar and D. Young: *Corros. Sci.*, 2000, vol. 42, pp. 861–883.
16. M. Welker, A. Rahmel, and M. Schütze: *Metall. Trans. A*, 1989, vol. 20, pp. 1541–1551.
17. K. Tjokro and D. J. Young: *Oxid. Met.*, 1995, vol. 44, pp. 453–474.
18. J. Klöwer, U. Brill, and M. Rockel: *Mater. Corros.*, 1997, vol. 48, pp. 511–517.
19. R. Elger and R. Pettersson: *Oxid. Met.*, 2014, vol. 82, pp. 469–490.
20. U. Krupp and H.-J. Christ: *Metall. Mater. Trans. A*, 2000, vol. 31, pp. 47–56.
21. L. E. Kindlimann and G. S. Ansell: *Metall. Trans.*, 1970, vol. 1, pp. 163–170.
22. B. A. Pint, M. J. Dwyer, and R. M. Deacon: *Oxid. Met.*, 2008, vol. 69, pp. 211–231.
23. D. L. Douglass: *Oxid. Met.*, 1995, vol. 44, pp. 81–111.
24. ASME-B36.10M-2018: *Welded and Seamless Wrought Steel Pipe*, The American Society of Mechanical Engineers, New York, NY, 2018.
25. Incoloy Alloy 800H & 800HT. (Special Metals Corporation, 2004), http://www.specialmetals.com/assets/smc/documents/alloys/incoloy/incoloy-alloys-800h-800ht.pdf.
26. ISO-21608:2012: *Corrosion of Metals and Alloys: Test Method for Isothermal-Exposure Oxidation Testing under High-Temperature Corrosion Conditions for Metallic Materials*, International Organization for Standardization, Geneva, Switzerland, 2012.
27. MATLAB-R2017b: The Mathworks Inc., Natick, Massachusetts, 2017.

28. J. Schindelin, I. Arganda-carreras, E. Frise, V. Kaynig, M. Longair, T. Pietzsch, S. Preibisch, C. Rueden, S. Saalfeld, B. Schmid, J.-y. Tinevez, D. J. White, V. Hartenstein, K. Eliceiri, P. Tomancak, and A. Cardona: *Nat. Methods*, 2012, vol. 9, pp. 676–82.
29. J.-O. Andersson, T. Helander, L. Höglund, P. Shi, and B. Sundman: *Calphad*, 2002, vol. 26, pp. 273–312.
30. J. Erneman, J.-O. Nilsson, H.-O. Andrén, and D. Tobjörk: *Metall. Mater. Trans. A*, 2009, vol. 40, pp. 539–550.
31. H. O. Pierson: *Handbook of Refractory Carbides and Nitrides: Properties, Characteristics, Processing, and Applications*, 1996.
32. A. L. Beardsley, C. M. Bishop, and M. V. Kral: *Mater. Perform. Charact.*, 2016, vol. 5, pp. 717–739.
33. J. I. Goldstein, D. E. Newbury, P. Echlin, D. C. Joy, C. E. Lyman, E. Lifshin, L. Sawyer, and J. R. Michael: *Scanning Electron Microscopy and X-Ray Microanalysis*, 3rd ed., 2003.
34. L. Tan, L. Rakotojaona, T. Allen, R. Nanstad, and J. Busby: *Mater. Sci. Eng., A*, 2011, vol. 528, pp. 2755–2761.
35. D. A. Porter, K. E. Easterling, and M. Y. Sherif: *Phase Transformations in Metals and Alloys*, 3rd ed., CRC Press, Boca Raton, FL, 2009.
36. M. Kikuchi, M. Kajihara, and S.-K. Choi: *Mater. Sci. Eng., A*, 1991, vol. 146, pp. 131–150.
37. A. J. Ramirez, J. C. Lippold, and S. D. Brandi: *Metall. Mater. Trans. A*, 2003, vol. 34A, pp. 1575–1597.
38. T.-H. Lee, S.-J. Kim, and S. Takaki: *Metall. Mater. Trans. A*, 2006, vol. 37, pp. 3445–3454.
39. H. Ono-Nakazato, K. Taguchi, T. Usui, K. Tamura, and Y. Tomatsu: *Metall. Mater. Trans. B*, 2001, vol. 32, pp. 1113–1118.
40. ISO-26146:2012: *Corrosion of Metals and Alloys: Method for Metallographic Examination of Samples after Exposure to High-Temperature Corrosive Environments*, International Organization for Standardization, Geneva, Switzerland, 2012.
41. M. Chase, Jr., C. Davies, J. Downey, Jr., D. Frurip, R. McDonald, and A. Syverud: *JANAF Thermochemical Tables*, 3rd ed., 1986.
42. G. C. Savva, G. C. Weatherly, and J. S. Kirkaldy: *Metall. Mater. Trans. A*, 1996, vol. 27, pp. 1611–1622.
43. I. C. Chen and D. L. Douglass: *Oxid. Met.*, 1990, vol. 34, pp. 473–496.
44. D. C. Montgomery and G. C. Runger: *Applied Statistics and Probability for Engineers*, 5th ed., John Wiley & Sons, Hoboken, NJ, 2011.
45. X. G. Zheng and D. J. Young: *Oxid. Met.*, 1994, vol. 42, pp. 163–190.
46. P. G. Shewmon: *Transformations in Metals*, McGraw-Hill, New York, 1969.
47. J. Litz, A. Rahmel, and M. Schorr: *Oxid. Met.*, 1988, vol. 30, pp. 95–105.
48. M. A. Harper, J. E. Barnes, and G. Y. Lai: in *Corrosion 97*, NACE International, Houston, TX, 1997.

List of Figures

699 **List of Tables**